MASARYKOVA
UNIVERZITA

PŘÍRODOVĚDECKÁ FAKULTA

Particle-in-cell simulace jiskrových událostí v polárních čepičkách pulzarů

Bakalářská práce

TATIANA RIEVAJOVÁ

Brno, jaro 2023

MASARYKOVA UNIVERZITA

PŘÍRODOVĚDECKÁ FAKULTA

Particle-in-cell simulace jiskrových událostí v polárních čepičkách pulzarů

Bakalářská práce

TATIANA RIEVAJOVÁ

Vedoucí práce: Mgr. Jan Benáček, Ph.D.

Ústav teoretické fyziky a astrofyziky

Brno, jaro 2023

MUNI
PŘÍRODOVĚDECKÁ
FAKULTA

Bibliografický záznam

Autor:	Tatiana Rievajová Přírodovědecká fakulta Masarykova univerzita Ústav teoretické fyziky a astrofyziky
Název práce:	Particle-in-cell simulace jiskrových událostí v polárních čepičkách pulzarů
Studijní program:	Fyzika
Obor:	Astrofyzika
Vedoucí práce:	Mgr. Jan Benáček, Ph.D.
Akademický rok:	2022/2023
Počet stran:	xiv + 36
Klíčová slova:	pulzar, particle-in-cell, simulace, jiskrová událost

Bibliographic record

Author:	Tatiana Rievajová Faculty of Science Masaryk University Department of theoretical physics and astrophysics
Title of Thesis:	Particle-in-cell simulations of sparking event in pulsar polar caps
Degree Programme:	Physics
Field of Study:	Astrophysics
Supervisor:	Mgr. Jan Benáček, Ph.D.
Academic Year:	2022/2023
Number of Pages:	xiv + 36
Keywords:	pulsar, particle-in-cell, simulation, sparking event

Abstrakt

Radiová emise pulsarů je úzce spjata s procesy v jejich magnetosféře. Rotující magnetické pole vytváří konvektivní elektrická pole, které jsou kompenzovány Goldreich-Julianovými proudy všude kromě oblastí v polárních čepičkách, které mají nízkou hustotu plazmatu. V těchto oblastech dochází k řadě plasmových nestabilit během takzvaných jiskrových událostí, které jsou zdrojem rádiové emise.

Konvektivní elektrické pole urychluje částice na ultrarelativistické rychlosti a ty poté emitují γ fotony, které se rozpadají na elektron-pozitronové páry. Cílem práce je analyzovat časový vývoj jiskrové události pomocí particle-in-cell kódu TRISTAN s nezbytnými implementacemi vzniku nových částic v gyrokinetické aproximaci v extrémně silných magnetických polí.

Abstract

The radio emission of pulsars is closely connected with processes in their magnetospheres. The rotating magnetic field creates a convective electric field that is compensated by Goldreich-Julian currents everywhere except the polar caps regions with low plasma density. In these regions, a number of instabilities occur during so-called sparking events which are the sources of radio emission.

The convective electric field accelerates the particles to ultrarelativistic velocities and the particles then emit γ-ray photons which decay in electron–positron pairs. The goal of the thesis is to analyse the time evolution of the sparking event using TRISTAN particle-in-cell code with necessary implementations of pair creation with gyrokinetic approximation in strong magnetic fields.

MASARYKOVA UNIVERZITA
PŘÍRODOVĚDECKÁ FAKULTA
KOTLÁŘSKÁ 2, 611 37 BRNO
IČ: 00216224
DIČ: CZ00216224

ZADÁNÍ BAKALÁŘSKÉ PRÁCE

Akademický rok: 2022/2023

Ústav:	Ústav teoretické fyziky a astrofyziky
Studentka:	Tatiana Rievajová
Program:	Fyzika
Specializace:	Astrofyzika

Ředitel *ústavu* PřF MU Vám ve smyslu Studijního a zkušebního řádu MU určuje bakalářskou práci s názvem:

Název práce:	Particle-in-cell simulace jiskrových událostí v polarních čepičkách pulzarů
Název práce anglicky:	Particle-in-cell simulations of sparking event in pulsar polar caps
Jazyk závěrečné práce:	angličtina

Oficiální zadání:
Pulzary jsou neutronové hvězdy a představují laboratoře pro studium přírodních zákonitostí v těch nejextrémnějších fyzikálních podmínkách. Neutronové hvězdy také vystupují v celé řadě dalších pozorovatelných astrofyzikálních úkazů jako jsou magnetary, akreující rentgenové zdroje, neutronové dvojhvězdy, mohou interagovat vzájemně nebo s černými děrami a jsou možným zdrojem rychlých rádiových záblesků. Rádiová emise pulzarů je zcela zásadně ovlivněna procesy probíhající v jejich magnetosférách. Standardní model magnetosféry je založen na formování Goldreichových-Julianových proudů, které kompenzují konvektivní elektrická pole vzniklá rotací extrémně silného magnetického pole. V otevřených magnetických smyčkách, ze kterých může plazma uniknou, je nízká hustota a tyto elektrické pole nejsou plně kompenzovány a mohou dosahovat 10^{12} V/m. V těchto oblastech probíhají jiskrové události, v nichž jsou částice urychlovány na ultrarelativistické rychlosti a produkují γ-fotony, které se rozpadají na elektron-pozitronové páry. Celý proces vytváří mraky částic plazmatu, které propagují podél magnetického pole a září v rádiové oblasti. Cílem práce je simulace vzniku takového mračna v extrémně silných elektrických polích pomocí jedno-dimenzionální particle-in-cell (PIC) simulací, které budou doplněny o fyzikální efekty potřebné k tomuto vzniku - vznik elektron-pozitronových párů. Výstupem práce je popis urychlování primárních částic, rozpad na sekundární částice, časového vývoje plasmatu, elektrických proudů a elektrického a magnetického pole. K simulování jiskrové události bude použit PIC kód Tristan. Postup: 1. Studium fyziky magnetosfér pulzarů, urychlování částic a vznik párů na kinetické úrovni plazmatu 2. Nastavení počátečních a okrajových podmínek v kódu Tristan, doplnění o potřebný numerický popis rozpadů. 3. Spuštění simulace na clusteru Metacentrum. 4. Analýza časového vývoje nestability. 5. Sepsání bakalářské práce se získanými výsledky.

Vedoucí práce:	Mgr. Jan Benáček, Ph.D.
Konzultant:	Mgr. Ing. arch. Petr Kurfürst, Ph.D.
Datum zadání práce:	4. 11. 2022
V Brně dne:	23. 5. 2023

Zadání bylo schváleno prostřednictvím IS MU.

Tatiana Rievajová, 21. 11. 2022
Mgr. Jan Benáček, Ph.D., 1. 12. 2022
RNDr. Luboš Poláček, 8. 12. 2022

Acknowledgements

I would like to thank my supervisor Mgr. Jan Benáček, Ph.D., for the help and assistance with my work. I am also very grateful for his guidance and the great amount of patience he had with me while writing this thesis. I appreciate all the extra opportunities he gave me to learn as much as possible about numerical code and plasma simulations.

I would also like to thank my family, who supported me during my studies. And a special thank you to my sister, for her moral support and understanding, without her I would have given up a long time ago.

Declaration

Hereby I declare that this paper is my original authorial work, which I have worked out on my own. All sources, references, and literature used or excerpted during elaboration of this work are properly cited and listed in complete reference to the due source.

Brno 23. 5. 2023 Tatiana Rievajová

Contents

Introduction

Neutron stars are the second densest objects in the universe after black holes. With their high density, small radius and possible strong magnetic field, they are a unique space laboratories for extreme conditions. Despite their not-so-recent discovery, there is still a lot we do not know about them.

Pulsars as one type of neutron stars have short rotating periods in the order of seconds and magnetic field up to 10^{12} G. Both high-energy and radio emission originates in their magnetosphere. The mechanism of pulsar radio emission is still quantitatively unknown. There are several theories and possible explanations but none was yet completely able to explain the observations.

In the last years with the advancement in numerical simulations, closer study of the radio emission processes was possible. The important work simulating the first self-consistent spark event and the pair creation with all necessary physical processes was done by Timokhin (2010, 2013) and Arendt and Eilek (2002). Some numerical studies and particle-in-cell simulations of pair cascade models were also presented recently by F. Cruz et al. (2022).

In the first chapter of this thesis, the main properties of pulsars as well as neutron stars are described with the general description of the sparking event. In the second chapter, the basic principles of the particle-in-cell method are presented with the specification of the TRISTAN code. In the third chapter, the implementations of the conditions of the pulsar magnetosphere with a simplified pair production model are presented. They are followed by analyses of two simulations of the spark event, one with periodic boundaries and one with absorbing boundary conditions.

1 Neutron stars

The existence of a neutron star was predicted by Baade and Zwicky (1934) long before its observation and just two years after the discovery of a neutron. Shortly after them Oppenheimer and Volkoff (1939) presented a simple equation of state to describe the internal structure of the neutron stars and to predict their mass, radius and density.

The general idea was that neutron stars were created after a supernova explosion and were composed primarily of neutrons. As such, they would have a very small radius and very high density. Pacini (1967) presumed that as magnetized rotating stars they were observable in X-rays. Nobody expected them to be a source of radio emission (Lyne and Graham-Smith 2012).

The first observation and confirmation of their existence came in 1967 by Jocelyn Bell Burnell and Antony Hewish. At first, the signal was considered as background noise from the Earth but the signal was repeating at regular intervals and they concluded it was connected to an oscillation of a neutron star (Hewish et al. 1968).

There are different types of neutron stars. The first ones are pulsars, neutron stars with periodical pulses of radio emission. Their rotational axis is not parallel with their magnetic axis (along which can be observed radio emission). As the star rotates the beam can be periodically observed from the Earth, a principle similar to a lighthouse (Lorimer and Kramer 2004).

The second type of neutron stars are magnetars, which are named for their strong magnetic field around 10^{15} G and complex magnetosphere. Next are millisecond pulsars with periods in the order of milliseconds. They are created in binary systems as a result of interaction between two stars (Lyne and Graham-Smith 2012).

1.1 Physical properties

When stars with an initial mass between 8 to 20 $M_\odot$ run out of nuclear fuel, their iron core collapse under its own gravitational force. If the mass of the core is greater than 1.4 $M_\odot$, the process results in a neutron star. The potential energy is released as a Type II supernova. The collapsed core, now a neutron star, has a mass between

1.4 to 2 $M_\odot$, with the upper limit still not precisely determined (Lyne and Graham-Smith 2012).

The exact equation of state for the neutron star is unknown and so is the radius for a given mass. Based on various theories and equations of state the expected radius is around 10 km. The limitation of the radius comes with the fast rotation and necessary balance between gravity and centrifugal force

$$\Omega^2 R = \frac{GM}{R^2}, \tag{1.1}$$

where Ω is the angular velocity, M is the mass, G is the gravitational constant and R is the radius. For period $P = 2\pi/\Omega$ we get

$$R_{\mathrm{max}} = \left(\frac{GMP^2}{4\pi^2}\right)^{1/3} = 1.5 \times 10^3 \left(\frac{M}{\mathrm{M}_\odot}\right)^{1/3} P^{2/3}\,\mathrm{km}. \tag{1.2}$$

For the fastest millisecond pulsar PSR J1748–2446ad (Hessels et al. 2006) with period 1.4 milliseconds the upper limit of the radius is 21 km for mass 1.4 $M_\odot$.

The internal structure and composition are different from the classical matter in other stars. The neutron stars consist of degenerate neutron gas with a very high density similar to the density of nuclear matter $10^{14}\,\mathrm{g\,cm^{-3}}$. Observations of young pulsars point to a solid crust and liquid interior with growing density towards the centre. However, the precise nature of the inner core is still debated and generally unknown. Above the core are superfluid neutrons which compose the largest part of the neutron star. The solid crust contains mostly free electrons (Lorimer and Kramer 2004).

1.2 Magnetars

Magnetars can be considered as a specific type of neutron stars or they can represent an extreme case of pulsars. Also, they are known as soft gamma-ray repeaters or anomalous X-ray pulsars. The main difference is in the magnetic field which is $10^{13} - 10^{15}$ G, much higher than a normal neutron star. They have a longer rotational period of up to 10 s. Emitted electromagnetic radiation is primarily in X-rays and gamma rays (Lyne and Graham-Smith 2012).

1.3 Milliseconds pulsars

The millisecond pulsars are named after their rotational period in the order of milliseconds. They are created in a binary system as a result of mass transfer onto the already created neutron star. Together with the mass the angular momentum is also transferred and causes a higher rotation speed. Before the interaction, the neutron star was in the process of decay and may have stopped emitting electromagnetic radiation but with the new material and faster rotation, it becomes a radio emitter once again which is why they are also called 'recycled' pulsars (Lyne and Graham-Smith 2012).

1.4 Pulsars

Pulsars are very highly magnetized neutron stars with the magnetic field $10^{10} - 10^{12}$ G. As mentioned before, the pulses are created when the beam of radiation emitted from the magnetic poles is in the line of sight of the observer, like a lighthouse effect. With time the rotation of the star, which is the same as the period of pulses, slows down because the rotational energy is transformed into high-energy radiation (Lorimer and Kramer 2004).

1.5 Magnetosphere

The surrounding of the pulsar is filled with plasma and dominated by the magnetic field. Plasma co-rotates with the pulsar up to the imaginary boundary called *light cylinder* where the velocity of plasma reaches the speed of light c. The distance of the light cylinder can be easily calculated as

$$R_{\mathrm{LC}} = \frac{c}{\Omega} = \frac{cP}{2\pi}, \tag{1.3}$$

with angular velocity Ω and period P (Hessels et al. 2006).

The existence of a light cylinder divides the magnetosphere into an equatorial and a polar region. The equatorial region is defined by closed magnetic field lines and the particles are trapped in this region. Whereas the particles in the open magnetic field lines in the polar region can flow out along those lines.

The simplest model of the magnetosphere with the magnetic dipole moment aligned with the rotational axis was described by Goldreich and Julian (1969). The rotating magnetic field induces a convective electric field which is balanced by a charge distribution creating electric field $\mathbf{E}$. If there is enough plasma, it results in a force-free state at position $\mathbf{r}$ with magnetic field $\mathbf{B}$

$$\mathbf{E} + \frac{1}{c}\left(\mathbf{\Omega} \times \mathbf{r}\right) \times \mathbf{B} = 0. \tag{1.4}$$

The force-free state can be found primarily in the closed magnetic field lines.

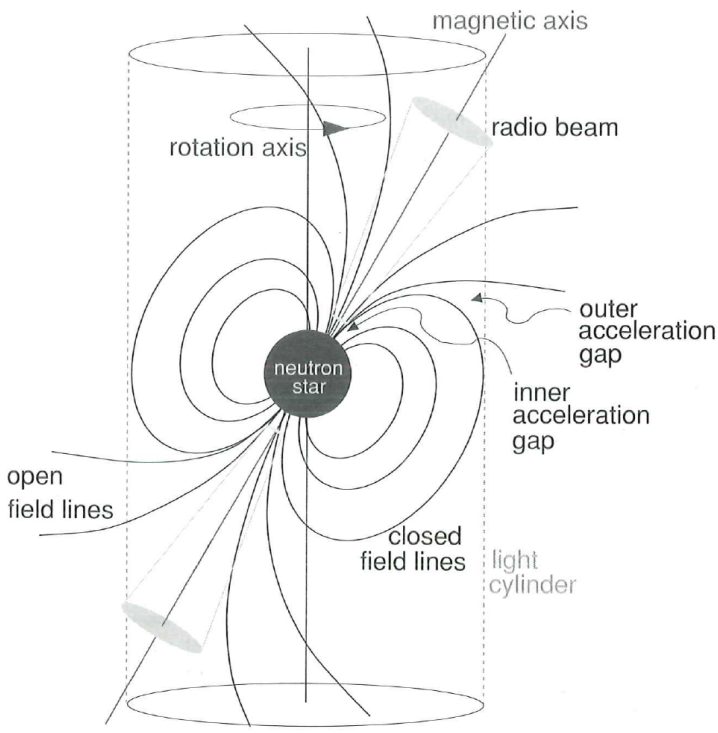

Figure 1.1: Model of the pulsar magnetosphere. The illustration is not to scale (Lorimer and Kramer 2004).

In Figure 1.1 are shown two acceleration gaps located in the polar region. In these gaps depleted of plasma the convective electric

field is no longer shielded and can then accelerate particles along the magnetic field lines to relativistic energies. Accelerated particles in the inner polar gap may be responsible for radio emission that we observe and the outer gap acceleration is the source of high energy radiation (Hessels et al. 2006).

1.5.1 Radio emission

The mechanism of radio emission is still not precisely understood. Normal radio emission, emission observed in older pulsars, is created in a smaller region within the polar cap in a spark event. The source of energy is the electric field induced by the rotating magnetic field. The electron-positron plasma accelerated by this electric field is assumed to originate in a *pair cascade*.

The basic principle of a pair cascade is shown in Figure 1.2. Electron or positron is accelerated along the magnetic field line and produces γ-ray photon which then can decay and create a new electron–positron pair. The energy of the photon must be at least twice the rest energy of an electron

$$E_\gamma \geq 2m_e c^2. \tag{1.5}$$

These secondary particles can too produce photons and thus creating an avalanche of secondary pair plasma. This secondary plasma is responsible for radio emission by coherent curvature radiation process (Eilek and Hankins 2016).

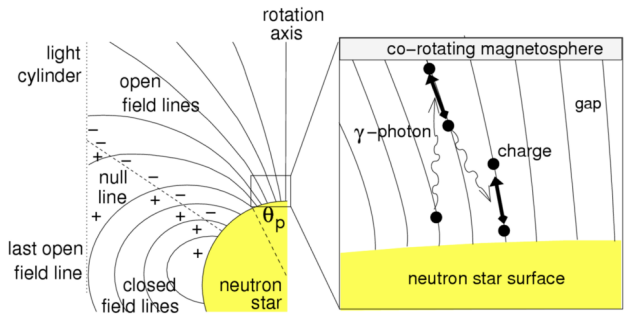

Figure 1.2: Goldreich-Julian model of pulsar magnetosphere with a scheme of electron-positron pair cascades at the polar gap region (Lorimer and Kramer 2004).

2 Particle-in-cell simulation

There are two different approaches to simulate a plasma – kinetic and fluid descriptions. Each one is used for different time and space scales. In a pulsar magnetosphere with collisionless plasma and a description of instabilities causing the radio emission on a microscopic level, the kinetic model is more relevant. In this thesis, we analyse a model of a pulsar polar cap sparking event using kinetic simulations of plasma.

In magnetohydrodynamic (MHD) simulation the plasma is described as a fluid and generally averaged quantities, for example, density or pressure are calculated. Particle-in-cell (PIC) simulation is based on the kinetic description of plasma and the position and velocity of each macroparticle are calculated.

2.1 Kinetic equations

The kinetic model describes plasma with a velocity distribution function $f(\mathbf{x}, \mathbf{v}, t)$. The time evolution is calculated by the Vlasov equation, collisionless Boltzmann equation, where particles feel only the Lorentz force

$$\left[\frac{\partial}{\partial t} + \mathbf{v} \cdot \frac{\partial}{\partial \mathbf{x}} + \frac{q_\alpha}{m_\alpha} \left(\mathbf{E} + \mathbf{v} \times \mathbf{B}\right) \frac{\partial}{\partial \mathbf{v}}\right] f_\alpha = 0, \tag{2.1}$$

where α represents the particle species present in the plasma, q is the charge and m is the mass of the particle.

The equation is solved indirectly by applying Liouville's theorem where in a collisionless plasma the distribution function f is invariant along the trajectories in the 6D phase space. It can be solved in a set of ordinary differential equations

$$\frac{d\mathbf{v}}{dt} = \frac{q}{m} \left[\mathbf{E} + \mathbf{v} \times \mathbf{B}\right], \qquad \frac{d\mathbf{r}}{dt} = \mathbf{v}. \tag{2.2}$$

Maxwell equations describe the electric and magnetic field

$$\begin{aligned} \nabla \cdot \mathbf{E} &= \frac{\rho}{\epsilon_0}, \\ \nabla \cdot \mathbf{B} &= 0, \\ \nabla \times \mathbf{E} &= -\frac{\partial \mathbf{B}}{\partial t}, \\ \nabla \times \mathbf{B} &= \mu_0 \mathbf{J} + \mu_0 \epsilon_0 \frac{\partial \mathbf{E}}{\partial t}, \end{aligned} \tag{2.3}$$

where ρ is the charge density and $\mathbf{J}$ is the electric current density, which can be calculated as

$$\begin{aligned} \rho &= \sum_\alpha q_\alpha \int dv^3 f_\alpha, \\ \mathbf{J} &= \sum_\alpha q_\alpha \int dv^3 \mathbf{v} f_\alpha. \end{aligned} \tag{2.4}$$

2.2 PIC method

Particle-in-cell method was first developed in the 1950s (Dawson 1983). To get the best result in the approximation in equations 2.2, a large number of particles is required. The solution can be challenging and instead of real particles, a fixed number of macroparticles is used. One macroparticle may represent a number of real particles which have similar trajectories in the phase space with the charge/mass ratio conserved. The simulation can support around 10^{12} macroparticles.

The shape of the macroparticle is not point-like but is described by a shape function which can be, for example, the Gaussian function. The velocity distribution function is then a superposition of individual macroparticles p with distribution f_p

$$f(\mathbf{x}, \mathbf{v}, t) = \sum_p f_p(\mathbf{x}, \mathbf{v}, t). \tag{2.5}$$

The collective behaviour of plasma and interaction between each particle is also modified. Particles interact only with the grid points as is shown in Figure 2.1. The movement of particles causes a change in the current density $\mathbf{J}$ deposited on the grid, which in turn causes

a change in the electric and magnetic field also calculated on the grid. The number of interactions N is reduced from $\sim N^2$ to N and the calculations are more efficient.

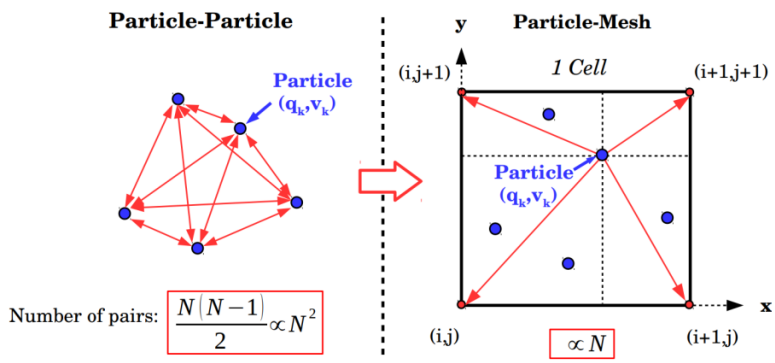

Figure 2.1: The main principle of the PIC method. Interactions between individual particles are replaced by interactions between the particle and the grid. The number of calculations then scales only linearly on the number of particles N (Cerutti 2015).

2.3 TRISTAN code

TRISTAN stands for TRI-dimensional STANford code. It is three dimensional, fully electromagnetic, relativistic code first introduced by O. Buneman and Storey (1985) for planet magnetosphere simulation. The code is also used in this thesis with some modifications to describe the conditions in the pulsar magnetosphere near the polar cap.

The basic computational scheme is shown in Figure 2.2. The code is fully self-consistent after the initial deposition of particles and fields on the mesh. First, the particles move and equations 2.2 are solved by a so-called particle push. Then, the particle current is interpolated to the grid where, lastly, the Maxwell equations 2.3 are solved by the field solver algorithm. With the interpolation of the fields from the grid to the positions of the particles, the loop starts again.

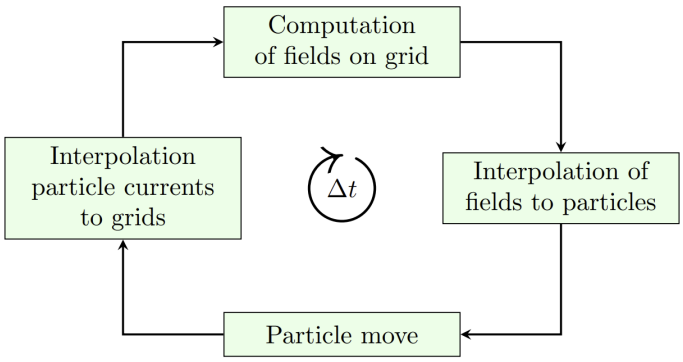

Figure 2.2: Computational scheme in PIC model (Benáček 2019).

TRISTAN code calculates with relative scales where $\epsilon_0 = 1$ and $\mu_0 = 1/c^2$. The symmetry between electric $\mathbf{E} = (e_x, e_y, e_z)$ and magnetic $\mathbf{B} = (b_x, b_y, b_z)$ field is expressed with components of the magnetic field multiplied by the speed of light $c\mathbf{B}$.

The Lorentz force from equations 2.2 and Maxwell equations 2.3 are solved with a leapfrog integration method. The position and velocity are staggered by half a time step, similarly the electric and magnetic field. The advantage is stability for oscillatory motion with a better conservation of energy.

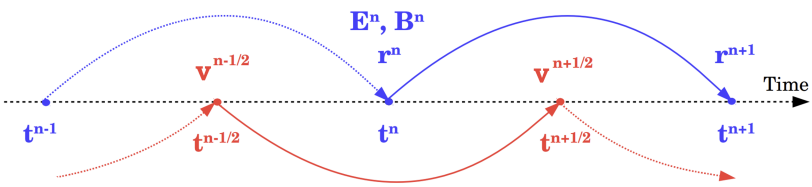

Figure 2.3: Representation of the leapfrog method. The position $\mathbf{r}$ and velocity $\mathbf{v}$ are staggered in time by a half-step (Cerutti 2015).

2.3.1 Particle push

The discretized differential equations 2.2 with a time step Δt are

$$\begin{aligned} \mathbf{v}^{\text{new}} &= \mathbf{v}^{\text{old}} + \frac{q\Delta t}{m}\left[\mathbf{E} + \frac{1}{2}\left(\mathbf{v}^{\text{new}} + \mathbf{v}^{\text{old}}\right) \times \mathbf{B}\right], \\ \mathbf{r}^{next} &= \mathbf{r}^{\text{present}} + \Delta t\, \mathbf{v}^{\text{new}}. \end{aligned} \tag{2.6}$$

The code uses the Boris push that is based on an idea to calculate the particle motion in three steps (Birdsall and Langdon 1991; Hockney and Eastwood 1981): the first half of the electric force

$$\mathbf{v}_0 = \mathbf{v}^{\text{old}} + \frac{q\mathbf{E}\Delta t}{2m}, \tag{2.7}$$

then the full magnetic rotation

$$\mathbf{v}_1 = \mathbf{v}_0 + 2\frac{\mathbf{v}_0 \times \mathbf{v}_0 \times \mathbf{b}_0}{1 + b_0^2} \times \mathbf{b}_0 \tag{2.8}$$

and the second half of the electric force

$$\mathbf{v}^{\text{new}} = \mathbf{v}_1 + \frac{q\mathbf{E}\Delta t}{2m}. \tag{2.9}$$

2.3.2 Current deposition

The direct current deposition scheme is applied in TRISTAN without using or calculating the charge density array. With the algorithm proposed by Villasenor and Oscar Buneman (1992), the charge density is conserved without any additional steps.

The integer grid points (i, j, k) represents the rounded positional value

$$i = \text{round}(x), \qquad j = \text{round}(y), \qquad z = \text{round}(z),$$

with the volume weighted distances

$$\delta x = x - i, \qquad \delta y = y - j, \qquad \delta z = z - k.$$

The electric field at a point (i, j, k) is modified by the current density $\mathbf{J} = (j_x, j_y, j_z)$

$$\begin{aligned}
e_x(i,j,k) &= e_x(i,j,k) - j_x \cdot cy \cdot cz, \\
e_x(i,j+1,k) &= e_x(i,j+1,k) - j_x \cdot \delta y \cdot cz, \\
e_x(i,j,k+1) &= e_x(i,j,k+1) - j_x \cdot cy \cdot \delta z, \\
e_x(i,j+1,k+1) &= e_x(i,j+1,k+1) - j_x \cdot \delta y \cdot \delta z,
\end{aligned}$$

$$\begin{aligned}
e_y(i,j,k) &= e_y(i,j,k) - j_y \cdot cx \cdot cz, \\
e_y(i,j+1,k) &= e_y(i,j+1,k) - j_y \cdot \delta x \cdot cz, \\
e_y(i,j,k+1) &= e_y(i,j,k+1) - j_y \cdot cx \cdot \delta z, \\
e_y(i,j+1,k+1) &= e_y(i,j+1,k+1) - j_y \cdot \delta x \cdot \delta z,
\end{aligned}$$

$$\begin{aligned}
e_z(i,j,k) &= e_z(i,j,k) - j_z \cdot cy \cdot cx, \\
e_z(i,j+1,k) &= e_z(i,j+1,k) - j_z \cdot \delta y \cdot cx, \\
e_z(i,j,k+1) &= e_z(i,j,k+1) - j_z \cdot cy \cdot \delta x, \\
e_z(i,j+1,k+1) &= e_z(i,j+1,k+1) - j_z \cdot \delta y \cdot \delta x,
\end{aligned}$$

where

$$cx = 1 - \delta x, \qquad cy = 1 - \delta y, \qquad cz = 1 - \delta z.$$

2.3.3 Field solver

The electric and magnetic fields are calculated from two time dependent Maxwell equations 2.3. As mentioned before they are staggered in time in the Yee algorithm (Yee 1966), used in TRISTAN as a field solver, and also in space. This intrinsically enforces the two divergence Maxwell equations.

The time change of **B** in one time step is

$$
\begin{aligned}
b_{\mathrm{x}}^{\mathrm{new}}(i,j,k) &= b_{\mathrm{x}}^{\mathrm{old}}(i,j,k) \\
&\quad + c\Delta t \left[\frac{e_{\mathrm{y}}(i,j,k+1) - e_{\mathrm{y}}(i,j,k)}{\Delta z} - \frac{e_{\mathrm{z}}(i,j+1,k) + e_{\mathrm{z}}(i,j,k)}{\Delta y} \right], \\
b_{\mathrm{y}}^{\mathrm{new}}(i,j,k) &= b_{\mathrm{y}}^{\mathrm{old}}(i,j,k) \\
&\quad + c\Delta t \left[\frac{e_{\mathrm{z}}(i+1,j,k) - e_{\mathrm{z}}(i,j,k)}{\Delta x} - \frac{e_{\mathrm{x}}(i,j,k+1) + e_{\mathrm{x}}(i,j,k)}{\Delta z} \right], \\
b_{\mathrm{z}}^{\mathrm{new}}(i,j,k) &= b_{\mathrm{z}}^{\mathrm{old}}(i,j,k) \\
&\quad + c\Delta t \left[\frac{e_{\mathrm{x}}(i,j+1,k) - e_{\mathrm{x}}(i,j,k)}{\Delta y} - \frac{e_{\mathrm{y}}(i+1,j,k) + e_{\mathrm{y}}(i,j,k)}{\Delta x} \right].
\end{aligned}
$$

For the numerical stability of the code, the change of the magnetic field is calculated in two half-advance time steps $\Delta t = 0.5$. This way, **B** is available for the particle push at the same time as **E**. The advance of the electric field is computed after the magnetic field half-advance in a similar way

$$
\begin{aligned}
e_{\mathrm{x}}^{\mathrm{new}}(i,j,k) &= e_{\mathrm{x}}^{\mathrm{old}}(i,j,k) \\
&\quad + c\Delta t \left[\frac{b_{\mathrm{y}}(i,j,k-1) - b_{\mathrm{y}}(i,j,k)}{\Delta z} - \frac{b_{\mathrm{z}}(i,j-1,k) + b_{\mathrm{z}}(i,j,k)}{\Delta y} \right], \\
e_{\mathrm{y}}^{\mathrm{new}}(i,j,k) &= e_{\mathrm{y}}^{\mathrm{old}}(i,j,k) \\
&\quad + c\Delta t \left[\frac{b_{\mathrm{z}}(i-1,j,k) - b_{\mathrm{z}}(i,j,k)}{\Delta x} - \frac{b_{\mathrm{x}}(i,j,k-1) + b_{\mathrm{x}}(i,j,k)}{\Delta z} \right], \\
e_{\mathrm{z}}^{\mathrm{new}}(i,j,k) &= e_{\mathrm{z}}^{\mathrm{old}}(i,j,k) \\
&\quad + c\Delta t \left[\frac{b_{\mathrm{x}}(i,j-1,k) - b_{\mathrm{x}}(i,j,k)}{\Delta y} - \frac{b_{\mathrm{y}}(i-1,j,k) + b_{\mathrm{y}}(i,j,k)}{\Delta x} \right].
\end{aligned}
$$

The stability of the algorithm is given by a Courant-Friedrichs-Lewy (CFL) condition in 3D (Courant, Friedrichs, and Lewy 1928)

$$
c\Delta t < \frac{\Delta x}{\sqrt{3}}, \tag{2.10}
$$

where Δt is the time step, Δx is a cell dimension and c is the speed of light in the simulation. The interpretation is that the time necessary for the signal to travel the distance of one cell cannot be less than one time step. In TRISTAN the values are normalized to $c = 0.5$, $\Delta t = 1$ and $\Delta x = 1$.

2.3.4 Boundary conditions

The outer boundaries of the computing domain are implemented based on the studied environment. In our simulations we use two types of boundaries. For the y and z axis we use periodic boundary conditions. In the x axis we use periodic or absorbing boundary conditions for both particles and fields.

3 Implementations and results

3.1 Implementations in the code

It was necessary to implement some modifications into the TRISTAN code to simulate conditions in the pulsar magnetosphere. Specifically, the gyrokinetic approximation for particles in a strong magnetic field, the addition of a convective electric field created by the rotation of the pulsar and a pair production model.

3.1.1 Gyrokinetic approximation

A gyromotion is a circular motion of charged particles perpendicular to the magnetic field lines. Stronger magnetic field B imply smaller radius of the gyromotion ρ

$$\rho = \frac{v_\perp m}{|q|B}, \tag{3.1}$$

where $v_\perp$ is the perpendicular velocity, m is the mass and q is the charge of the particle.

The perpendicular component of the momentum is promptly radiated as synchrotron photons and the particles have only the parallel velocity (Timokhin 2010). Because of the rapid radiation of the perpendicular momentum in a strong magnetic field, we can calculate only with the parallel component throughout the simulation.

The velocity of particles at the beginning of the simulation is given by a velocity distribution function in a general direction with both parallel and perpendicular components. In the first time step, a projection into the direction of the magnetic field is calculated

$$\mathbf{v}_\parallel = \frac{\mathbf{v} \cdot \mathbf{B}}{|\mathbf{B}|^2}\,\mathbf{B} \tag{3.2}$$

and the perpendicular velocity is set to zero. The demonstration of the implementation is in Figure 3.1. At the beginning, the velocity of the particles is distributed in both axis and in the next time step the particles have only the velocity parallel to the magnetic field in the x axis.

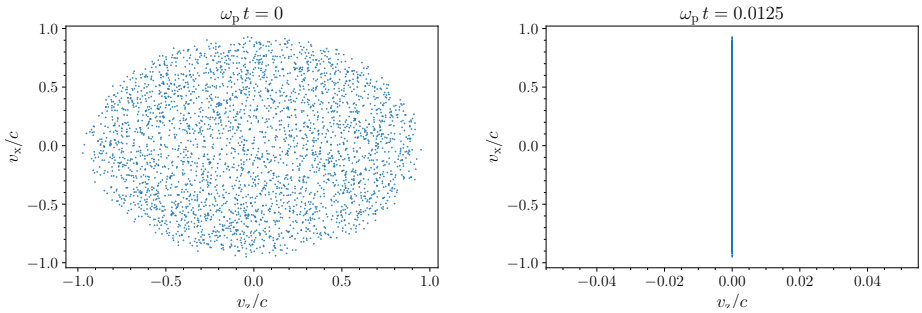

Figure 3.1: Test of the gyrokinetic approximation. Distribution of velocity in x and z axis in the beginning is on the left. In the next time step after the projection into the direction of the magnetic field is on the right.

3.1.2 Convective electric field

The numerical implementation of the Maxwell equations 2.3 calculates only the local change in the electric and magnetic field but the rotation of the pulsar creates a convective electric field that we have to take into account. The value of the convective electric field is established in the configuration of the simulation and is added up in every time step to the local electric field.

3.1.3 Pair creation

The fundamental process of *pair creation* is described in section 1.5.1. The pairs are created by the absorption of photons in the magnetic field in quantum electrodynamics (QED) processes. In this thesis, we use a simplified model of pair production.

The new pair is created when an electron or a positron is accelerated and its Lorentz factor reaches a threshold value γ_{th}. Secondary particles are created in the same place as the primary particle (photons have a zero mean free path) and the energy of the photon is equally split between them (Fábio Cruz, Grismayer, and Silva 2021).

3.2 Numerical Cerenkov radiation

In simulations with relativistic plasma and high energy particles, a numerical Cerenkov radiation can be created. The problem is in the Yee

method used as a field solver, where high frequency waves propagate slower than the speed of light. Relativistic particles near the speed of light are therefore faster than their radiation. The problem can be solved by using a Friedman filter as described in Greenwood et al. (2004).

The normalized intensity of the electric field in 2D simulation is shown in Figure 3.2. The dimensions were $100\Delta \times 8\Delta \times 100\Delta$ and the parameters of the simulation were $e = 0.003125$, $m_\mathrm{e} = 0.0625$, $c = 0.5$, $v_\mathrm{tb} = 1c$ and $\omega_\mathrm{p}\Delta t = 0.0125$. On the left is the intensity without the Friedman filter. We can see sharp changes from one cell to the next with a regular pattern. On the right graph was a simulation with the same conditions and parameters with the addition of the Friedman filter $\theta = 0.1$. The oscillations are reduced and the development is more smooth without any sudden changes between two grid cells.

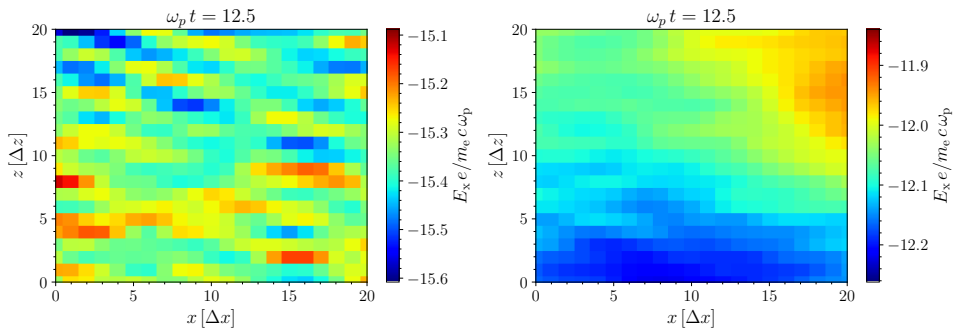

Figure 3.2: Comparison of the normalized intensity of the electric field without the Friedman filter (left) and with the Friedman filter $\theta = 0.1$ (right).

3.3 Simulations

We performed two 1D simulations of electron–positron plasma, actual 3D simulations with one dominant axis parallel to the magnetic field. The only difference was in boundary conditions. Simulation I had periodic boundaries representing a closed magnetic field line. Simulation II had absorbing boundaries simulating open magnetic field lines.

Common parameters of both simulations are in Table 3.1. We start with one electron and one positron per cell and a plasma frequency $\omega_{\mathrm{p,i}}$. The number of particles increased during the simulation due to the pair creation. Consequently, a new plasma frequency was calculated ω_{p} with the maximum number of particles in the simulation.

The electron skin depth associated with ω_{p} is $d_{\mathrm{e}} = c/\omega_{\mathrm{p}} \approx 11.1\,\Delta$. With a typical frequency for electron–positron plasma $f_{\mathrm{p}} = 1\,\mathrm{GHz}$, the electron skin depth is $d_{\mathrm{e}} = c/(2\pi f_{\mathrm{p}}) \approx 4.77\,\mathrm{cm}$. The length of the simulations in x axis is then approximately 25.8 m.

Table 3.1: Common parameters of both simulations.

Parameter	Value
Dimensions	$6000\Delta \times 8\Delta \times 8\Delta$
Particle density per cell n_{i}	1
Speed of light c	0.5
Permittivity of the vacuum ϵ_0	1
Mass of the particles $m_{\mathrm{e}} = m_{\mathrm{i}}$	0.0625
Elementary charge e	0.003125
$\omega_{\mathrm{p,i}}\Delta t$	0.0125
$\omega_{\mathrm{p}}\Delta t$	0.045
$\omega_{\mathrm{ce}}/\omega_{\mathrm{pe}}$	1000000
Particle thermal velocity v_{tb}	$1c$
Friedman filter θ	0.1
γ_{th}	200
Energy ratio in decay	0.1
Magnetospheric current density	$(0.01, 0, 0)$

A ratio between electron cyclotron frequency and electron plasma frequency $\omega_{\mathrm{ce}}/\omega_{\mathrm{pe}}$ corresponds directly to the value of the magnetic field. The threshold for the Lorentz factor γ_{th} in both simulations is $\gamma_{\mathrm{th}} = 200$ which corresponds to the physical value $\gamma_{\mathrm{th}} \sim 10^7$ (F. Cruz et al. 2022). Our model of the pair creation depends mainly on the value of γ_{th}. With higher value, the particles in Simulation II leave the simulation before they are accelerated enough to create secondary particles.

When a primary particle reaches a Lorentz factor γ_{th} a part of its kinetic energy is used to create secondary particles with both kinetic and rest energy. The amount of kinetic energy used in this process is determined by the *energy ratio in decay* parameter. A particle at rest with charge $e = 1$ and mass $m = 1$ is in one time step accelerated by the convective electric field $E_{\text{con}} = 0.01$ to one hundredth the speed of light. The convective electric field is set by the *magnetospheric current density* parameter.

3.3.1 Kinetic energy

The time evolution of the total kinetic energy in simulations is shown in Figure 3.3. Both start with an acceleration of particles and an increase in kinetic energy. Around the time step $\omega_{\text{p}} t = 40$, the first pair creation starts.

In Simulation I, the kinetic energy after the pair creation starts to oscillate. The amplitude gradually decreases due to the compensation of the convective electric field by the particle current. When the electric field is completely screened the kinetic energy is stabilized with no new spark events.

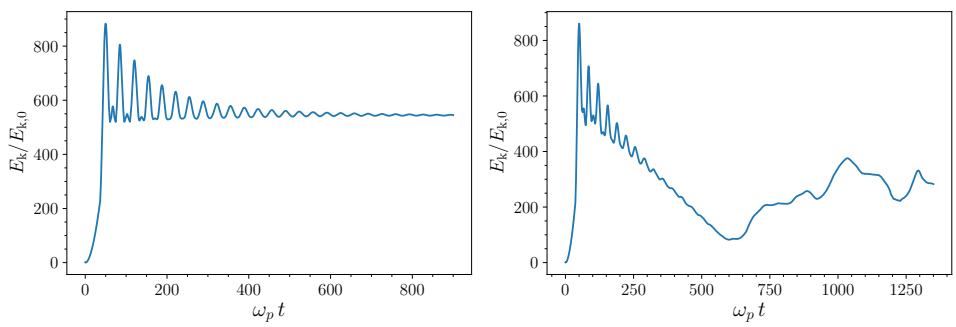

Figure 3.3: Time evolution of the kinetic energy normalized to the initial kinetic energy. On the left is Simulation I with periodic boundaries. On the right is Simulation II with absorbing boundaries.

In Simulation II, the evolution of the kinetic energy is the same as in Simulation I until around the time $\omega_{\text{p}} t = 600$. In the first spark event, oscillations and compensation of the electric field are the same,

with different stabilized values of the kinetic energy because of the outflow of the particles from the simulation. When there are not enough particles to screen the electric field anymore a new spark event starts and the kinetic energy rises again.

3.3.2 Energy of the electric field

In Figure 3.4 is the time evolution of the electric energy E_x in the axis parallel to the magnetic field. In the beginning, the energy of the electric field increases because of the convective electric field E_{con} added in every time step. After the start of the pair cascade, the electric field is gradually compensated and starts to oscillate with a change of polarity. The oscillations in the energy of the electric field E_x correspond to the oscillations in the kinetic energy E_k.

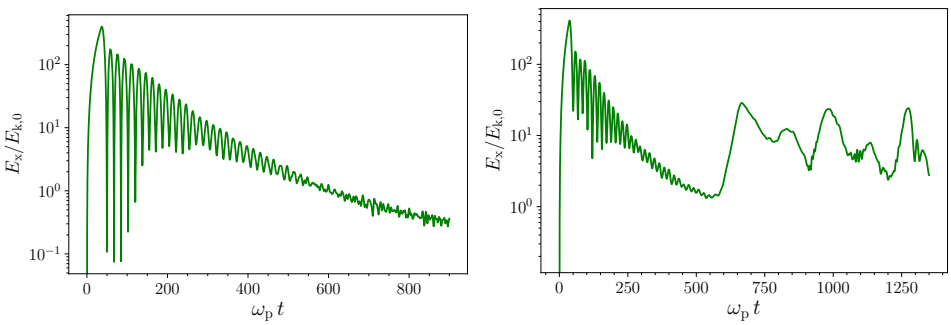

Figure 3.4: Time evolution of the electric energy in x axis normalized to the initial kinetic energy. Simulation I is on the left and Simulation II is on the right.

To better understand the correspondence we compare the electric energy and the kinetic energy from Simulation I as shown in Figure 3.5. With the increase in the electric energy, the particles are accelerated until around time $\omega_p t = 40$ first secondary particles are created. A gentle stagnation in the kinetic energy at the start of the pair creation is caused by the transformation of the kinetic energy of the primary particle to the rest energy of the secondary particles.

A decrease in the electric energy corresponds to an increase in the kinetic energy. The more accelerated the particles are the bigger is the cur-

rent screening the electric field. When the kinetic energy reaches a maximum, for example, in time $\omega_p t = 50$, the electric field changes its polarity. With the changed polarity the particles are accelerated in the opposite direction.

The little rise in the kinetic energy, for example, between $\omega_p t = 60$ and $\omega_p t = 75$ is caused by a significant change in the direction of movement of particles.

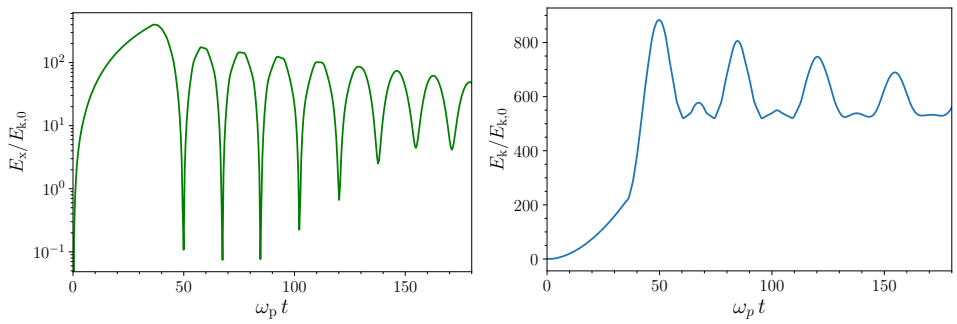

Figure 3.5: Comparison of the energy of the electric field with the kinetic energy during the pair cascade in Simulation I. Both are normalized to the initial kinetic energy $E_{k,0}$.

3.3.3 Spark event in the phase space

The distribution of electrons in the phase space is shown in Figure 3.6. At the beginning of the simulation, the electrons are distributed the same way in both simulations.

In the middle row, we can see accelerated particles with Lorentz factor near the γ_{th} in the whole length of the simulation. This means that the pair creation starts at the same time in every grid cell of the simulation. That is because the conditions are the same and as soon as a particle reaches the threshold value γ_{th} secondary particles are created. The bottom horizontal line in the phase space represents the primary particles. The rest of the horizontal lines are the consecutive decays of the primary particles. The first spark event is in both cases in the whole length of the simulation.

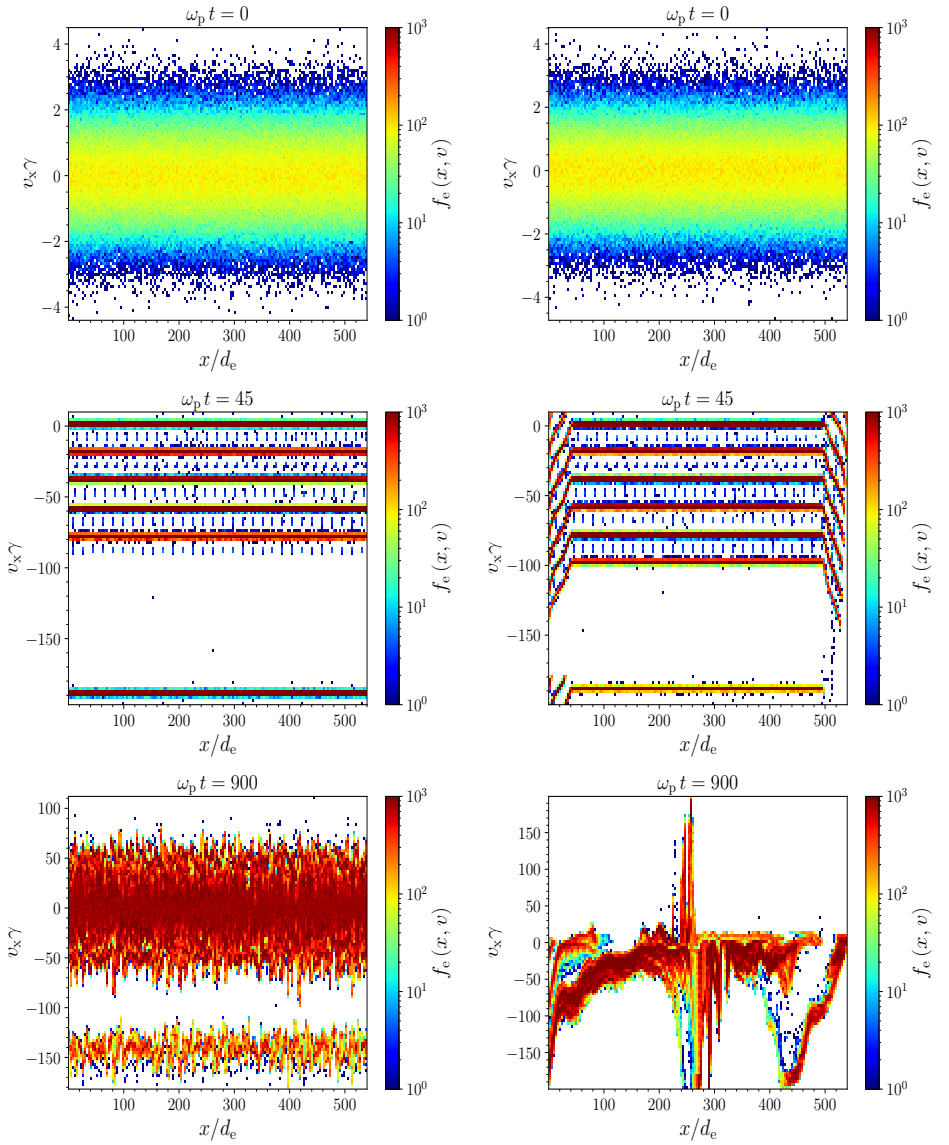

(a) Simulation I **(b)** Simulation II

Figure 3.6: A phase space for electrons in three different parts of the simulation. At the top is the initial distribution of electrons. In the middle is the beginning of the pair cascade. At the bottom is the stabilization in Simulation I and new spark event in Simulation II.

At the bottom left subfigure is the end of Simulation I with stabilized kinetic energy and completely screened electric field. The primary particles are still separated in velocity from the secondary particles. The secondary particles are no longer in separated horizontal lines but they are blended together.

At the bottom right is the new spark event in Simulation II. The new pair creation is different and does not happen in the whole length of the simulation at the same time. Only in certain places is the accelerating electric field not screened and bunches of particles are created.

3.3.4 Intensity of the electric field

The time evolution of the intensity of the electric field is shown in Figure 3.7. In both cases, we start with the same value in every cell of the simulation. The initial intensity of the electric field is zero.

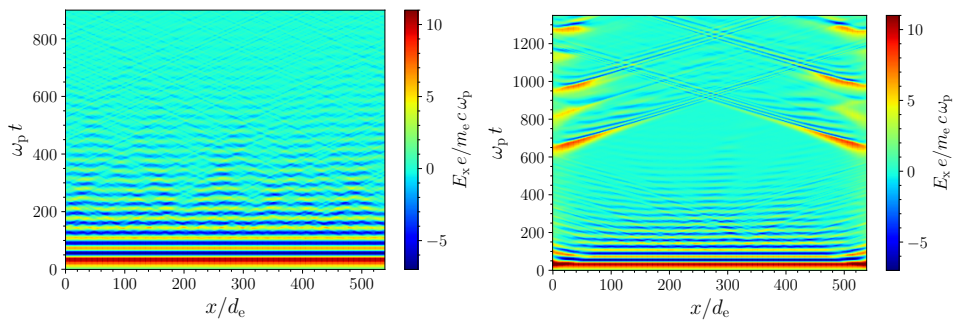

Figure 3.7: Time evolution of the intensity of the electric field across the simulation. On the left is Simulation I and on the right is Simulation II.

In Simulation I, the oscillations following the start of the pair cascade are uniform throughout the whole length of the simulation. The homogeneity is reflected in the horizontal lines in the phase space in Figure 3.6. With time, the amplitude of the oscillations decreases as the particles compensate the electric field and the homogeneity is disturbed.

In Simulation II with absorbing boundaries, the intensity on the edges is slightly higher because there is a smaller number of particles screen-

ing the electric field. After the first pair cascade, the evolution is similar to the one in Simulation I. Around time $\omega_p t = 600$ plasma on both edges is depleted of particles and the convective electric field is no longer screened. In this region starts a new sparking event.

3.3.5 Evolution of the created bunches

The time evolution of an electron and positron density with the bunches of particles created in the pair cascade are in Figure 3.8 and Figure 3.9. In both simulations we start with one electron and positron per cell and the first increase in density is along the whole simulation at the same time. The reason is the same as with the intensity of the electric field, the conditions are the same in every cell.

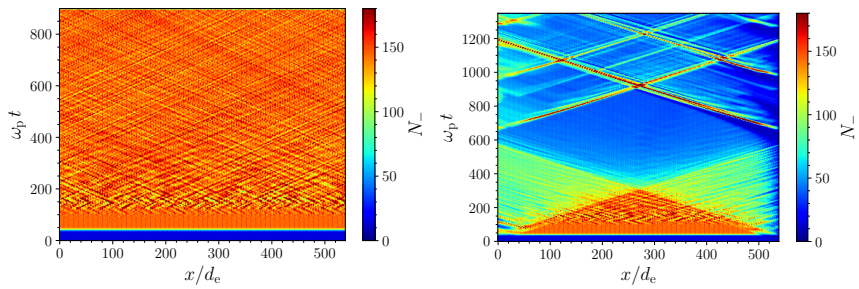

Figure 3.8: Time evolution of the density of electrons in Simulation I on the left and Simulation II on the right.

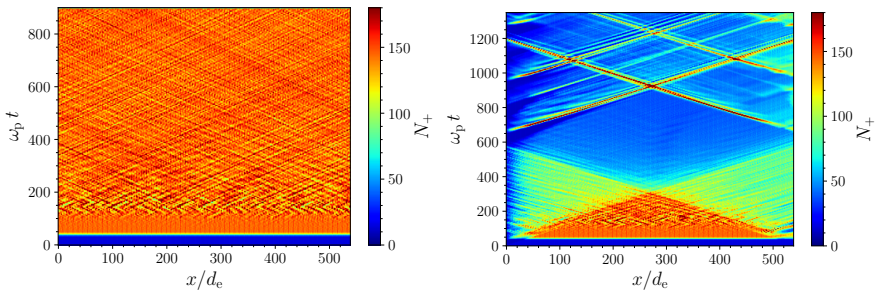

Figure 3.9: Time evolution of the density of positrons in Simulation I on the left and Simulation II on the right.

In Simulation I, the movement of the bunches of particles across the simulation is a straight line indicating a constant velocity. A different situation is in Simulation II. The particles created in the first spark event leave the simulation and at time $\omega_p t = 600$ in the new spark event the bunches are created only at the edges.

3.3.6 Dispersion properties

Dispersion of electrostatic waves along the x axis is shown in Figure 3.10. We took the whole length of the x axis and an average value in the y and z axis. The electric intensity was saved every 10 time steps and its absolute value is shown in (ω, k) space. The data were processed with a cosine window filter.

The cutoff frequency ω is lower than the plasma frequency because it decrease as $\omega = \langle \gamma^{-3} \rangle \, \omega_p$. The horizontal line with the wave number k close to zero is caused by the addition of the constant convective electric field in every time step. In both simulations, relativistic Langmuir wave branches can be seen as hyperbolas.

While in Simulation I the branch is relatively narrow in frequency, in Simulation II we can see a set of overlying branches. This is caused by the variation in density and plasma frequency during the spark event which changes the frequency of the Langmuir waves in Simulation II. Simulation I is filled with particles and their density, as well as the Langmuir wave frequency, is saturated.

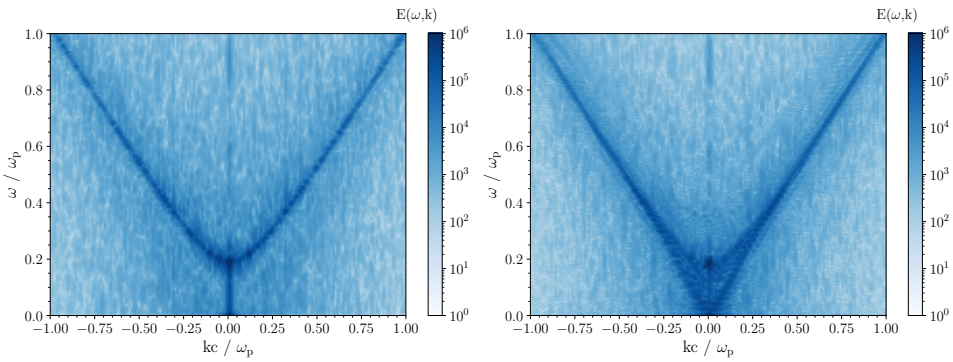

Figure 3.10: The absolute value of intensity E_x along the x-axis in (ω, k) space. Simulation I is on the left and Simulation II is on the right.

Conclusion

The aim of this thesis was to analyse the time evolution of the spark event. Two spark events in 1D particle-in-cell (PIC) simulations with different boundary conditions were compared.

In the first part, I presented today's knowledge of neutron stars and more specifically pulsars, their properties and a fundamental model of the magnetosphere. The processes in the magnetosphere are closely connected with radio and high-energy emissions. Different plasma instabilities and mechanisms of radiation are responsible for the X-rays and radio emission observations.

One of the possible instability behind the radio emission called sparking event was described in section 1.5.1. In the spark event the particles in the magnetosphere plasma are accelerated to ultra-relativistic velocities and γ photons are emitted. The decay of these photons creates electron–positron pairs and starts a pair cascade responsible for radio emission.

In the second part, I describe the fundamental principles of the PIC simulations and the TRISTAN code numerical algorithms used in this work. Specific implementations simulating the conditions in the pulsar magnetosphere were presented in the next part.

The sparking event was simulated in Simulation I with periodic boundary conditions representing closed magnetic field lines. After the first spark event with pair creation and oscillations in the kinetic and electric energy (Figure 3.3 and 3.4) there was a stabilization of the simulation with no new pair creation.

Simulation II with absorbing boundary conditions represents open magnetic field lines with possible particle outflow. In these conditions, the time evolution of the first spark event was similar to Simulation I until the first saturation. Unlike in the first simulation, the spark event was repeated with pair creation primarily at the edges of the simulation (Figure 3.8 and 3.9) where the plasma can outflow first.

For future improvements a pair creation model with decay probabilities and a non-trivial photon mean free path calculation could be implemented into the TRISTAN code. The analysis of the electromagnetic waves created during the sparking event requires a longer simulation.

Appendix

Here is a simplified pair creation model implemented in Fortran into the TRISTAN code .

```fortran
module qed

    contains

    subroutine threshhold_decay(n1,n2,n_stop,n_other,n_other_stop,bx,by,bz,x,y,z,u,v,w)
        use config, only: nptl, c, g_thresh, me, decay_energy_ratio
        use init, only: random
        implicit none

        real(8), dimension(:,:,:):: bx,by,bz
        integer :: n, n1,n2, n_stop, n_other,n_other_stop, sigma
        real(8), dimension(nptl):: x,y,z,u,v,w
        integer :: i,j,k
        real(8) :: g, E, dE, B, dv, v_new, v_old, E_ratio, vx, vy, vz, r

        do n = n1, n2
            g = c/sqrt(c*c-u(n)*u(n)-v(n)*v(n)-w(n)*w(n))
            !write(*,*) "gamma, g_thresh", g, g_thresh

            if (g.gt.g_thresh) then
                E = (g-1)*me*c*c
                dE = decay_energy_ratio*E

                ! Check weather a new pair can be created
                if (dE.lt.(2*me*c*c)) then
                    STOP "Emitted energy is not large enough to creat new pair"
                end if

                dv = c/((E-dE)/(me*c*c)+1)
                v_new = sqrt(c*c-dv*dv)
                v_old = sqrt(u(n)*u(n)+v(n)*v(n)+w(n)*w(n))

                ! Energy loss of primary particle
```

```
                    !write(*,*) "velocity decrease", v_new/v_old

                    u(n) = v_new/v_old*u(n)
                    v(n) = v_new/v_old*v(n)
                    w(n) = v_new/v_old*w(n)

                    ! Calculate velocity of secondary particle
                    E_ratio = 2*me*c*c/dE
                    !write(*,*) "Energy ratio", E_ratio
                    v_new = c*sqrt(1-E_ratio*E_ratio)

                    i = int(x(n))
                    j = int(y(n))
                    k = int(z(n))
                    B = sqrt(bx(i,j,k)*bx(i,j,k)+by(i,j,k)*by(i,j,k)+bz(i,j,k)*bz(i,j,k))

                    vx = v_new*bx(i,j,k)/B
                    vy = v_new*by(i,j,k)/B
                    vz = v_new*bz(i,j,k)/B

                    !write(*,*) "new particle velocity", vx, vy, vz

                    if (vx.gt.0) then
                        sigma = 1
                    else
                        sigma = -1
                    end if

                    n2 = n2+1
                    if (n2.gt.n_stop) then
                        STOP "Cannot add secondary particle, buffer is not large enough"
                    end if

                    u(n2) = sigma*vx
                    v(n2) = sigma*vy
                    w(n2) = sigma*vz
                    x(n2) = x(n)
                    y(n2) = y(n)
                    z(n2) = z(n)

```

```
                n_other = n_other+1
                if (n_other.gt.n_other_stop) then
                    STOP "Cannot add secondary particle, buffer is not large enough"
                end if

                u(n_other) = sigma*vx
                v(n_other) = sigma*vy
                w(n_other) = sigma*vz
                x(n_other) = x(n)
                y(n_other) = y(n)
                z(n_other) = z(n)

            end if
        end do

    end subroutine threshhold_decay



end module qed
```

Bibliography

Arendt Paul N., Jr. and Jean A. Eilek (Dec. 2002). "Pair Creation in the Pulsar Magnetosphere". In: 581.1, pp. 451–469. DOI: 10.1086/344133.

Baade, W. and F. Zwicky (May 1934). "Cosmic Rays from Supernovae". In: *Proceedings of the National Academy of Science* 20.5, pp. 259–263. DOI: 10.1073/pnas.20.5.259.

Benáček, Jan (2019). "Particle-in-cell simulations and analytical study of the processes generating radio solar bursts". PhD thesis. Masaryk university, Brno. URL: https://is.muni.cz/th/mmrz3/.

Birdsall, C. and A. Langdon (1991). *Plasma physics via computer simulation*. 1st ed. CRC Press.

Buneman, O. and L. R. O. Storey (Mar. 1985). *Simulations of fusion plasmas by A 3-D, E-M particle code*. Final Report, 1 Jan. - 31 Dec. 1984 Stanford Univ., CA. Space, Telecommunications and Radioscience Lab.

Cerutti, Benoît (2015). *Particle-in-cell simulations*. Accessed: 5-3-2019.

Courant, R., K. Friedrichs, and H. Lewy (1928). "On the Partial Difference Equations of Mathematical Physics". In: *Mathematische Annalen* 100, pp. 32–74.

Cruz, F. et al. (May 2022). "Model of pulsar pair cascades in non-uniform electric fields: Growth rate, density profile, and screening time". In: *Physics of Plasmas* 29.5, 052902, p. 052902. DOI: 10.1063/5.0085847.

Cruz, Fábio, Thomas Grismayer, and Luis O. Silva (Feb. 2021). "Kinetic Model of Large-amplitude Oscillations in Neutron Star Pair Cascades". In: 908.2, 149, p. 149. DOI: 10.3847/1538-4357/abd2c0.

Dawson, John M. (Apr. 1983). "Particle simulation of plasmas". In: *Reviews of Modern Physics* 55.2, pp. 403–447. DOI: 10.1103/RevModPhys.55.403.

Eilek, Jean A. and Timothy H. Hankins (June 2016). "Radio emission physics in the Crab pulsar". In: *Journal of Plasma Physics* 82.3, 635820302, p. 635820302. DOI: 10.1017/S002237781600043X. arXiv: 1604.02472 [astro-ph.HE].

Goldreich, Peter and William H. Julian (Aug. 1969). "Pulsar Electrodynamics". In: 157, p. 869. DOI: 10.1086/150119.

Greenwood, Andrew D. et al. (Dec. 2004). "On the elimination of numerical Cerenkov radiation in PIC simulations". In: *Journal of Computational Physics* 201.2, pp. 665–684. DOI: 10.1016/j.jcp.2004.06.021.

Hessels, J. W. T. et al. (June 2006). "A Radio Pulsar Spinning at 716 Hz". In: *American Astronomical Society Meeting Abstracts #207*. Vol. 207. American Astronomical Society Meeting Abstracts, 209.07, p. 209.07.

Hewish, A. et al. (Feb. 1968). "Observation of a Rapidly Pulsating Radio Source". In: 217.5130, pp. 709–713. DOI: 10.1038/217709a0.

Hockney, R. W. and J. W. Eastwood (1981). *Computer Simulation Using Particles*. New York: McGraw-Hill.

Lorimer, D. R. and M. Kramer (2004). *Handbook of Pulsar Astronomy*. Vol. 4. Cambridge University Press.

Lyne, Andrew and Francis Graham-Smith (2012). *Pulsar Astronomy*. 4th ed. Cambridge Astrophysics. Cambridge University Press.

Oppenheimer, J. R. and G. M. Volkoff (Feb. 1939). "On Massive Neutron Cores". In: *Physical Review* 55.4, pp. 374–381. DOI: 10.1103/PhysRev.55.374.

Pacini, F. (Nov. 1967). "Energy Emission from a Neutron Star". In: 216.5115, pp. 567–568. DOI: 10.1038/216567a0.

Timokhin, A. N. (Nov. 2010). "Time-dependent pair cascades in magnetospheres of neutron stars - I. Dynamics of the polar cap cascade with no particle supply from the neutron star surface". In: 408.4, pp. 2092–2114. DOI: 10.1111/j.1365-2966.2010.17286.x.

– (Mar. 2013). "The complex charm of the pulsar magnetosphere". In: *Neutron Stars and Pulsars: Challenges and Opportunities after 80 years*. Ed. by Joeri van Leeuwen. Vol. 291, pp. 273–278. DOI: 10.1017/S174392131202385X.

Villasenor, John and Oscar Buneman (1992). "Rigorous charge conservation for local electromagnetic field solvers". In: *Computer Physics Communications* 69.2, pp. 306–316. DOI: https://doi.org/10.1016/0010-4655(92)90169-Y.

Yee, Kane (May 1966). "Numerical solution of initial boundary value problems involving maxwell's equations in isotropic media". In: *IEEE Transactions on Antennas and Propagation* 14.3, pp. 302–307. DOI: 10.1109/TAP.1966.1138693.